

# Geophysical Research Letters<sup>®</sup>

## RESEARCH LETTER

10.1029/2024GL111590

### Key Points:

- Periodic magnetic strength enhancements are observed during the bow shock crossing of the MMS spacecraft
- Multi-spacecraft analysis supports the scenario of shock ripples rather than the shock reformation process
- The surface waves alter the shock geometry, modulating the reflected ions and whistler wave packets

### Correspondence to:

X.-Z. Zhou,  
xzhou@pku.edu.cn

### Citation:

Li, J.-H., Zhou, X.-Z., Wang, S., Liu, Z.-Y., Zong, Q.-G., Yao, S.-T., et al. (2024). Bow shock ripples and their modulation of whistler wave packets: MMS observations. *Geophysical Research Letters*, 51, e2024GL111590. <https://doi.org/10.1029/2024GL111590>

Received 24 JUL 2024

Accepted 9 SEP 2024

## Bow Shock Ripples and Their Modulation of Whistler Wave Packets: MMS Observations

Jing-Huan Li<sup>1</sup> , Xu-Zhi Zhou<sup>1</sup> , Shan Wang<sup>1</sup>, Zhi-Yang Liu<sup>2</sup> , Qiu-Gang Zong<sup>1,3</sup> , Shu-Tao Yao<sup>4</sup> , Anton V. Artemyev<sup>5</sup> , Yoshiharu Omura<sup>6</sup> , Li Li<sup>1</sup> , Chao Yue<sup>1</sup> , and Quan-Qi Shi<sup>4</sup> 

<sup>1</sup>Institute of Space Physics and Applied Technology, Peking University, Beijing, China, <sup>2</sup>Institut de Recherche en Astrophysique et Planétologie, CNES-CNRS Université Toulouse III Paul Sabatier, Toulouse, France, <sup>3</sup>State Key Laboratory of Lunar and Planetary Sciences, Macau University of Science and Technology, Macau, China, <sup>4</sup>Shandong Provincial Key Laboratory of Optical Astronomy and Solar-Terrestrial Environment, Institute of Space Sciences, Shandong University, Weihai, China, <sup>5</sup>Institute of Geophysics and Planetary Physics, University of California, Los Angeles, CA, USA, <sup>6</sup>Research Institute for Sustainable Humanosphere, Kyoto University, Uji, Japan

**Abstract** The terrestrial bow shock is the boundary where supersonic solar wind slows down abruptly near the magnetopause. The shock front geometry could be modulated by surface waves to form rippled structures, which impact the acceleration process of the solar wind particles. However, the rippled structures are hard to be identified unambiguously due to the similar signatures in single-spacecraft observations between rippled shocks and reforming shocks. Here, we utilize the four-spacecraft observations from the MMS mission to investigate an event of quasi-perpendicular bow shock crossing. The periodic oscillations of shock normal directions and normal velocities support the scenario of surface wave propagation in the tangential direction. We also reconstruct the shock profile along the normal direction, and its monotonic shape further excludes the occurrence of shock reformation. These ripples are found to modulate the reflected ions and whistler wave packets, which adds to the complexity of the bow shock plasma environments.

**Plain Language Summary** Collisionless shocks are ubiquitous structures in the space and astrophysical plasma environments where significant energy conversion occurs between electromagnetic energy, kinetic energy, and thermal energy. These structures often exhibit nonstationary signatures, from which important information on the associated plasma dynamics can be extracted. In this paper, we report the spacecraft observations of a bow shock crossing with periodic enhancements of the magnetic field strength. Such signatures have been previously attributed either to the rippled shock structures or to the shock reformation process. These two potential processes are examined via simultaneous observations at four different locations, which shows the periodic oscillations of the local shock normal directions indicative of rippled rather than reforming shocks. We also show that the rippled shocks could spatially modulate the reflected ions and whistler wave packets, so they can also be detected periodically by the spacecraft. This phenomenon has been reported on other planets across a wide range of Mach numbers, indicating that the shock ripples, universal in the plasma universe, play a critical role in impacting particle dynamics and shock evolution processes.

## 1. Introduction

Shock waves, often abbreviated as shocks, are ubiquitous structures formed when the relative velocity between the fluid flow and an obstacle exceeds the characteristic maximum sound speed. These structures, characterized by abrupt changes in fluid pressure, temperature, and density, are often accompanied by substantial energy transfer and dissipation processes (Malkov et al., 2011). In an ordinary gas medium, particle collisions are usually responsible for the transfer from kinetic energy to thermal energy. In the collisionless space plasma environments, however, the energy transfer becomes more complicated and is mainly achieved via wave-particle interactions. Multiple mechanisms, such as dispersive radiation (Krasnoselskikh et al., 2002), particle reflection (Kennel et al., 1985), and quasi-static fields (Scudder et al., 1986), have all been posited to account for the macroscopic energy transfer near the shocks. Ultimately, they are believed to culminate in microscopic, randomly phased or coherent wave-particle interactions (Pitña et al., 2021; Wilson et al., 2014a, 2014b). Therefore, it is important to investigate the various plasma waves and their interplay with different particle populations for a comprehensive understanding of the energy transfer and dissipation in this critical region.

© 2024, The Author(s).

This is an open access article under the terms of the Creative Commons Attribution License, which permits use, distribution and reproduction in any medium, provided the original work is properly cited.

Shock properties are intrinsically determined by a few key parameters, including  $\theta_{Bn}$ , the angle between the shock normal direction and upstream magnetic field, and the Alfvén Mach number  $M_A$ , the ratio between the upstream flow velocity along the shock normal direction and the Alfvén speed. In quasi-perpendicular shocks ( $\theta_{Bn} > 45^\circ$ ) with well-defined foot and ramp structures (Kennel et al., 1985), whistler waves are believed to play an essential role in the energy dissipation process (Lalti et al., 2022). These waves are usually generated by micro-instabilities associated with the reflected ions, and they can sometimes be phase standing in the upstream flow to maintain a stable shock front, especially when  $M_A$  is small (Krasnoselskikh et al., 2002). For those events with sufficiently high  $M_A$ , the imbalance between the field steepening and the dissipation processes could lead to the formation of a nonstationary shock front (Morse et al., 1972), which is believed to accommodate more significant particle heating or acceleration (Caprioli et al., 2014; Umeda et al., 2009).

The observations of nonstationary shock fronts may be attributed either to shock reformation (Krasnoselskikh et al., 2002) or to surface waves (Lowe & Burgess, 2003). Two models have been proposed to elucidate the shock reformation processes. The first model is called the gradient catastrophe model, which suggests that the shock ramp can break up into two sub-ramps when the shock profile surpasses a specific gradient threshold (Krasnoselskikh et al., 2002). This theory is supported by the observations of electron-scale structures inside the shock ramp (Dimmock et al., 2019). An alternative model suggests that new shock fronts emerge in association with the ion reflection and accumulation at the foot region (Matsukiyo & Scholer, 2006; Scholer et al., 2003), which is supported by the periodic magnetic field enhancements commonly observed near the bow shocks of Earth (Madanian et al., 2021), Mars (Madanian et al., 2020), and Saturn (Sulaiman et al., 2015).

On the other hand, surface waves have also been observed in a variety of space plasma boundaries including but not limited to the plasmapause (He et al., 2020), the magnetopause (Archer et al., 2019, 2021), and the bow shock (Johlander et al., 2016). The surface wave generation on the bow shock could be attributed to the ion cyclotron instability, drift mirror instability (Winske & Quest, 1988), and/or shear-driven instability (Omidi et al., 2021). As surface waves propagate along the shock surface (Lowe & Burgess, 2003), the shock geometry could be significantly modified to cause periodic magnetic field oscillations (Omidi et al., 2021). Therefore, the observational signatures of the shock surface waves are quite similar to those of the shock reformation process, and their differentiation often relies on simultaneous measurements from multiple spacecraft.

The shock surface waves have been recently identified by measurements from the four-spacecraft constellation missions such as Cluster (Moullard et al., 2006) and MMS (Magnetospheric Multiscale mission) (Gingell et al., 2017). The high-resolution particle measurements from the MMS satellites have further indicated the association between rippled, quasi-perpendicular shocks and the ion phase-space holes in the downstream region (Johlander et al., 2016, 2018). In these studies, the periodic observations of ion phase-space holes are interpreted as the back-and-forth crossings of the bow shock. However, given the finite width of the foot region, it is also possible that the spacecraft only traverses the shock foot and the unperturbed solar wind further upstream, although the corresponding observational signatures have never been explored.

Here, we examine the multi-spacecraft observations of a quasi-perpendicular bow shock outside the terrestrial dawnside magnetopause. In this event, the local normal directions and normal propagation speeds of the shock front are determined as functions of time via the MDD (minimum directional difference) and STD (spatio-temporal difference) techniques (Shi et al., 2005, 2006). They both show periodic oscillations, which are unambiguous evidence for the formation of surface waves. The surface waves alter the shock front geometry and consequently, modulate the spacecraft measurements. As a result, the reflected ions and whistler wave packets, commonly detected around the foot region, appear periodically due to the back-and-forth motion of the spacecraft between the foot region and the unperturbed solar wind.

## 2. Results

### 2.1. Overview

On 02 May 2021, the four-spacecraft MMS constellation traveled across the terrestrial bow shock at  $[-0.8, -22.7, 3.9] R_E$  in Geocentric Solar Eclipse (GSE) coordinates. The MMS data utilized in this study are obtained from the Fast Plasma Investigation (FPI) and Flux Gate Magnetometer (FGM) instruments (Pollock et al., 2016; Russell et al., 2016; Torbert et al., 2016). Figure 1 offers a 1.5-min overview of the MMS1 observations during this event. Figure 1a shows the variations of the magnetic field strength,  $B_t$ , which increases from 8.3 to 31 nT to indicate the

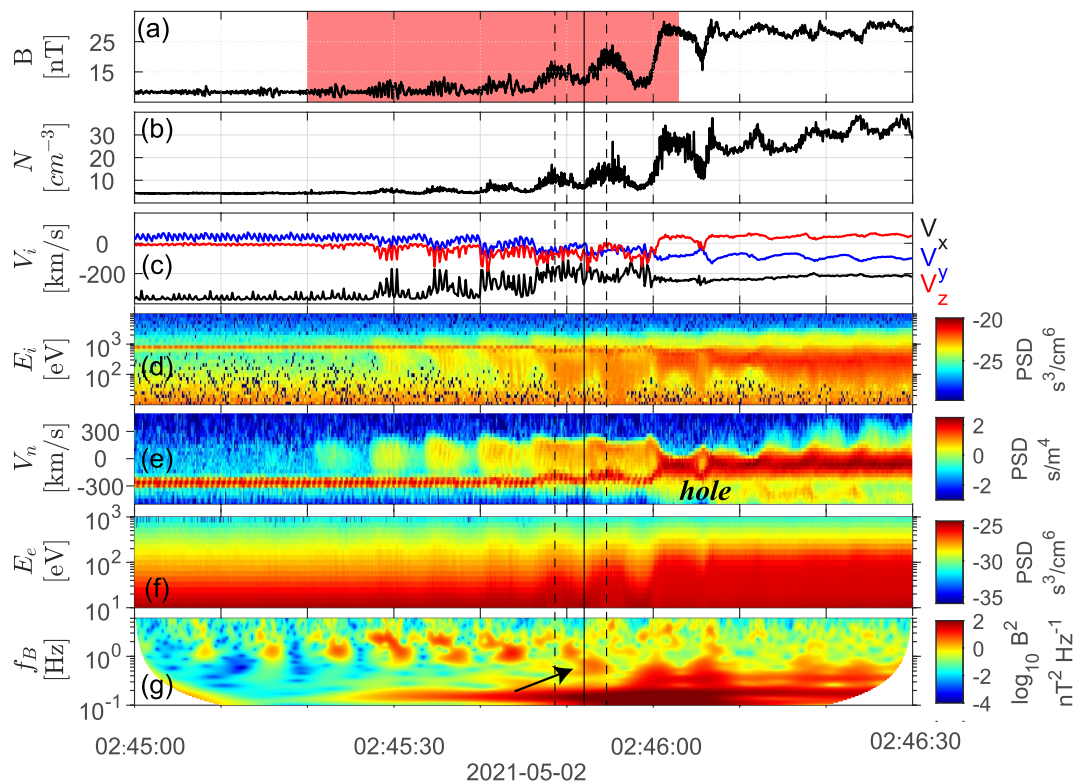


**Figure 1.** Overview of the MMS1 spacecraft observations across the quasi-perpendicular bow shock. (a) Magnetic field strength. (b) Plasma number density. (c) The three GSE components of the ion bulk velocity. (d) The energy spectrum of the ion PSDs. (e) The one-dimensional, normal-velocity spectrum of the ion PSDs. (f) The energy spectrum of the electron PSDs. (g) Wavelet power spectra of the magnetic field.

gradual penetration of the spacecraft across the bow shock from the foreshock solar wind toward the magnetosheath. The enhancements of the particle number density (see Figure 1b) and the decrease of the ion bulk velocity (see Figure 1c) are also consistent with the spacecraft entry to the magnetosheath.

To determine the basic properties of the bow shock, we average the spacecraft measurements during two stable intervals, 02:45:00–02:45:26 UT and 02:46:10–02:46:20 UT, to obtain the magnetic field and ion bulk velocity in the upstream (hereinafter referred to by subscript u) and downstream (subscript d) regions, respectively. The field variations,  $\Delta \mathbf{B} = \mathbf{B}_d - \mathbf{B}_u$ , and velocity variations,  $\Delta \mathbf{v} = \mathbf{v}_d - \mathbf{v}_u$ , are then used to estimate the shock normal direction (Schwartz, 1998), given by

$$\mathbf{n}_{bs} = \pm \frac{(\Delta \mathbf{B} \times \Delta \mathbf{v}) \times \Delta \mathbf{B}}{|(\Delta \mathbf{B} \times \Delta \mathbf{v}) \times \Delta \mathbf{B}|}. \quad (1)$$

The resulting normal direction,  $\mathbf{n}_{bs} = [0.64, -0.74, 0.22]$ , deviates from the  $\mathbf{B}_u$  direction,  $[-0.37, -0.81, -0.45]$  by an angle  $\theta_{Bn} = 78^\circ$ , indicative of a quasi-perpendicular bow shock. Note that the estimated normal direction is insensitive to the choice of averaging intervals. We also apply a few different techniques described in Schwartz (1998) to estimate the normal direction, and the results (not shown) only deviate from  $\mathbf{n}_{bs}$  by a few degrees, confirming the accuracy of our analysis. One may also determine, based on the Rankine-Hugoniot relation for the continuity of tangential electric field, the shock normal speed  $V_{bs,n}$  in the spacecraft rest frame,

$$V_{bs,n} = \frac{|\mathbf{n}_{bs} \times (\mathbf{V}_d \times \mathbf{B}_d - \mathbf{V}_u \times \mathbf{B}_u)|}{|\Delta \mathbf{B}|}, \quad (2)$$

which is calculated to be approximately 10.5 km/s. This speed indicates a sunward motion of the shock, which is consistent with the gradual entry of the spacecraft into the magnetosheath. Based on this shock speed and the ion bulk velocity projected along  $\mathbf{n}_{bs}$ , we also compute the Alfvén Mach number  $M_A \sim 3.3$ .

During the shock penetration of the spacecraft (the shadowed interval in Figure 1, before the  $B_t$  peak), periodic variations of  $B_t$  are observed with a period of  $\sim 8$  s. The large-amplitude  $B_t$  variations also modulate the particle behavior, manifested by the synchronized enhancement of the particle number density and reduction of the ion flow speed (see Figures 1b and 1c). Figure 1d presents the energy spectrum of the ion phase space densities (PSDs). Before the shadowed interval, the ion PSDs peak sharply at  $\sim 1$  keV, which corresponds to the energy of the solar wind bulk velocity in Figure 1c. As time proceeds, there gradually emerges another population, and their appearances are well correlated to the periodic  $B_t$  enhancements. This new population is the reflected ions, which can be better visualized in the one-dimensional, normal-velocity spectrum (Figure 1e, see the population with higher velocities than the background solar wind population at  $\sim -300$  km/s). The overlapping of the two ion populations indicates the availability of free energy for wave excitation, which has been invoked to explain the frequent observations of the whistler waves near the foot of the bow shock (Lalti et al., 2022). Meanwhile, the electron energy spectrum in Figure 1f also exhibits a clear correlation between electron PSD enhancements and  $B_t$  variations.

Figure 1g displays the wavelet power spectrum of the magnetic field, in which the large-amplitude field variations discussed above are manifested by the peak of the wave power at  $\sim 0.12$  Hz (or the wave period of  $\sim 8$  s). Intermittent, high-frequency waves can also be identified at  $\sim 1$ – $3$  Hz. These high-frequency waves appear every  $\sim 8$  s (also see Figure 1a), and therefore, they must be modulated by or coupled with the low-frequency waves. To better understand the relationship between these waves, it is important to first determine their properties.

## 2.2. Whistler Waves

We first focus on the properties of the high-frequency waves. Based on the phase shift between different field components, these waves are found to be right-hand polarized in the spacecraft frame. We next apply the phase difference analysis (Dudok de Wit et al., 1995; Li, Zhou, Liu, Wang, Artemyev, et al., 2024) on the four-spacecraft field measurements between 02:45:27 and 02:45:32, to determine the wave vectors and consequently the wave phase velocities as functions of frequency. The averaged wave phase velocity within the frequency range of interest equals  $\mathbf{v}_w = [74.6, -100.1, -72.5]$  km/s in GSE coordinates, which deviates from the upstream  $\mathbf{B}_u$  by  $\sim 53^\circ$ . Given that the solar wind velocity  $\mathbf{v}_{sw}$  equals  $[-371.8, 41.1, -8.3]$  km/s, the waves propagate sunward at the speed of  $\sim 450$  km/s in the plasma rest frame, with its right-handed polarization unchanged after considering the Doppler effect. The analyses for other wave packets yield similar results. Therefore, these high-frequency wave packets are identified to be oblique whistler waves, which have been widely reported in the upstream region of the terrestrial bow shocks (L. B. Wilson, 2016; Li, Zhou, Liu, Wang, Artemyev, et al., 2024; Li, Zhou, Liu, Wang, Omura, et al., 2024; Wang et al., 2024). These waves, as discussed in the introductory section, are often believed to be strongly associated with the reflected ion population (Lalti et al., 2022). This is consistent with the nearly synchronized observations between the high-frequency waves and the reflected ions (compared Figures 1e–1g). Interestingly, the whistler waves could occur further upstream without the discernible presence of the reflected ions (see Figures 1e and 1g, between 02:45:00 and 02:45:20). This could be attributed to the sunward propagation of the waves away from their source near the foot region, although it is also possible that the reflected ions are too tenuous in the upstream region to exceed the noise level of the FPI instrument.

## 2.3. Surface Waves

We next analyze the properties of the low-frequency waves. Figure 2a is a replica of Figure 1a showing the magnetic field strength, except that the shadowed interval (with the most significant wave activity at  $\sim 0.12$  Hz) is selected to perform a detailed analysis. To eliminate the impact of high-frequency waves, the field measurements from the MMS satellites are averaged within a running window of 2.5 s, and the results are displayed in Figure 2b. Obviously, they show similar trends due to the minor inter-spacecraft separation. We next employ the MDD method (Shi et al., 2005) on the four-spacecraft magnetic field data, to determine at each time the direction along which the directional derivative of the magnetic field maximizes. The eigenvalues of the field gradients, displayed in Figure 2d, suggest that the maximum eigenvalue  $\lambda_1$  always exceeds the intermediate eigenvalue  $\lambda_2$  by at least one order of magnitude. The eigenvectors corresponding to  $\lambda_1$  represent the local normal directions  $\mathbf{n}_l$ , which vary

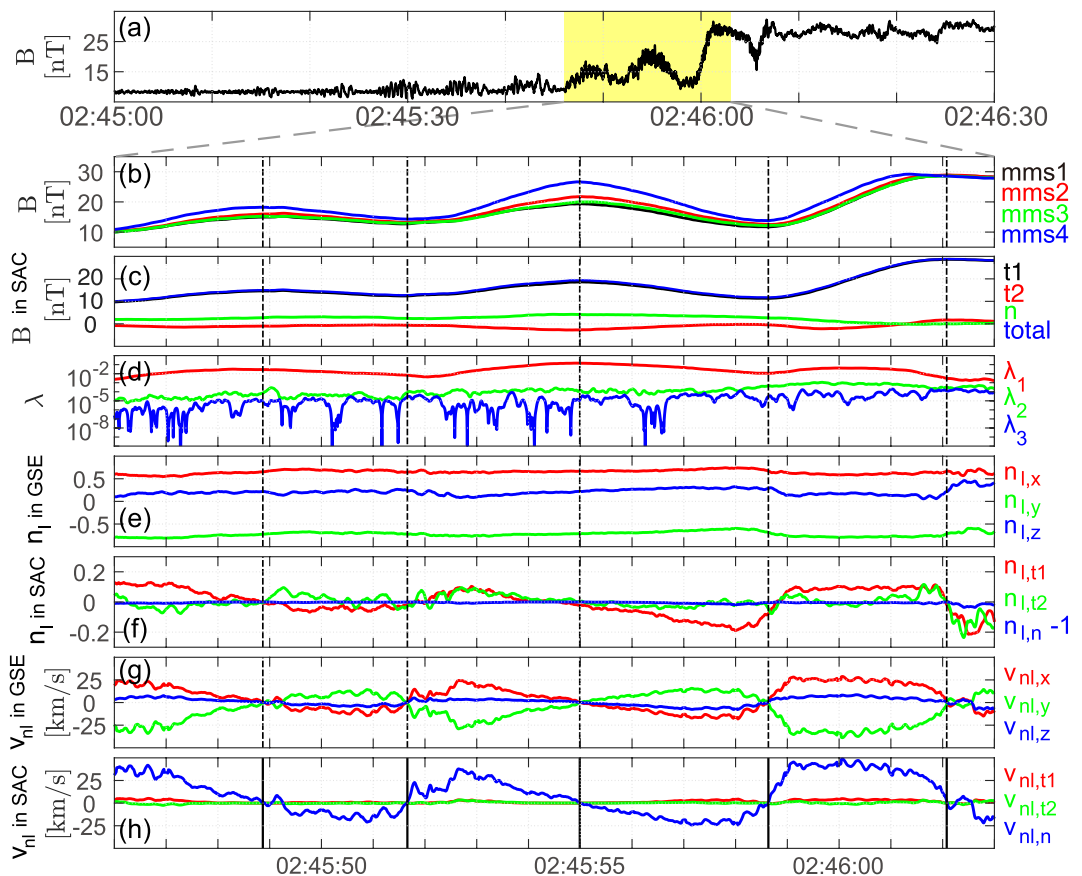


**Figure 2.** MDD and STD analysis of the shock surface waves. (a) Magnetic field strength. (b) 2.5-s running-averaged magnetic field strength of four spacecraft. (c) MMS1 observations of the magnetic field in SAC coordinates. (d) The three eigenvalues of the MDD analysis (e)–(f) The eigenvectors that correspond to the maximum eigenvalues, displayed in GSE and SAC coordinates, respectively (g)–(h) The STD analysis results of the normal propagation velocity, in GSE and SAC coordinates, respectively.

only slightly with time (see Figure 2e, in GSE coordinates). These results further confirm that the shock front can be treated as a quasi-1D structure (Wang et al., 2019). The average  $\mathbf{n}_l$  direction during this time interval,  $\mathbf{n}_{avg}$ , equals  $[0.65, -0.72, 0.21]$ , which deviates by approximately  $1^\circ$  from the  $\mathbf{n}_{bs}$  direction obtained through Equation 1, thereby justifying both approaches.

We next organize the observations in a shock-aligned coordinate (SAC) system composed of the  $\mathbf{e}_n$ ,  $\mathbf{e}_{t1}$ , and  $\mathbf{e}_{t2}$  axes, where  $\mathbf{e}_n$  is defined by  $\mathbf{n}_{avg}$ ,  $\mathbf{e}_{t2}$  is defined by the cross product of  $\mathbf{e}_n$  and  $\mathbf{B}_u$ , and  $\mathbf{e}_{t1}$  completes the orthogonal triad (Johlander et al., 2016). Since  $\mathbf{n}_{avg}$  is nearly perpendicular to  $\mathbf{B}_u$ , the  $\mathbf{e}_{t1}$  axis is approximately field-aligned in the upstream region. Figure 2c presents the MMS1 observations of the magnetic field in SAC coordinates, which indeed shows the dominance of  $B_{t1}$  component (black line). We next project the  $\mathbf{n}_l$  vectors in Figure 2e into the SAC system, and the temporal variations of the three components are shown in Figure 2f. One may easily find that the  $\mathbf{n}_l$  component along  $\mathbf{e}_n$ ,  $n_{l,n}$ , is always near 1, which indicates that the local normal direction varies only slightly. On the other hand, the  $\mathbf{n}_l$  component along  $\mathbf{e}_{t1}$ ,  $n_{l,t1}$ , oscillates in the same tone as the low-frequency waves, with its value approaching zero near the  $B_t$  extrema (indicated by the black vertical lines). We also utilize the four-spacecraft measurements to compute the structural motion via the STD method (Shi et al., 2006). For the quasi-1D structure in this event, the STD method yields the temporal variation of the propagation speed  $v_{nl}$  along the local normal direction,  $\mathbf{n}_l$ . Figures 2g and 2h show the  $v_{nl}$  velocity in GSE and SAC coordinates, respectively. They also display periodic oscillations with reversals near the  $B_t$  extrema.

The periodic oscillations of the shock normal direction and the normal propagation velocity can be understood by the presence of surface waves on the shock front. Let us assume a tangential propagation of the surface waves

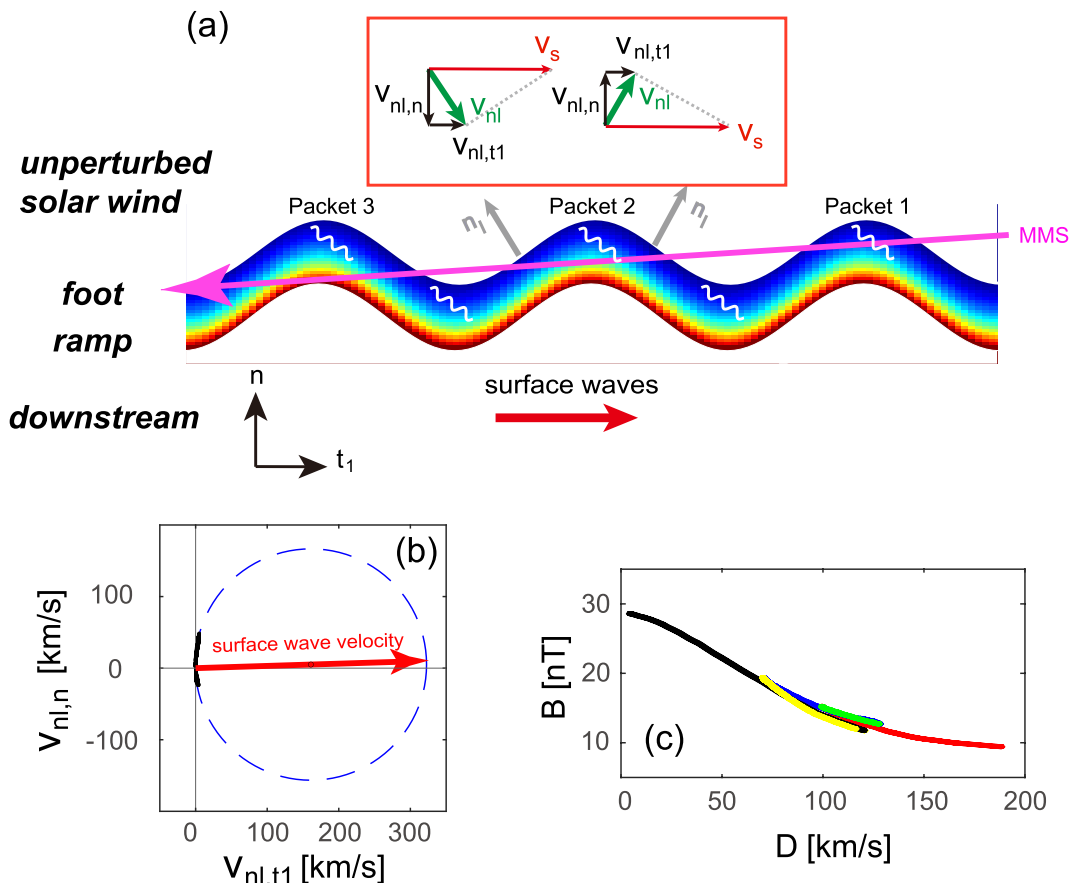


**Figure 3.** Properties of the shock surface waves. (a) Illustration of MMS trajectory across the rippled bow shock. The relationship between the velocity vectors are given in the inset. (b) Two-dimensional projections of the vector-end points for  $v_{nl}$  (black dots). They are all located very close to the best-fitted spherical surface represented by the blue circle, of which the diameter (red arrow) corresponds to the surface wave velocity. (c) Profile of the magnetic field strength along the shock normal direction.

(Johlander et al., 2016; Moullard et al., 2006) at the speed of  $v_s$  along the  $\mathbf{e}_{t1}$  axis. As illustrated in Figure 3a, the projection of  $v_s$  along the local normal direction  $\mathbf{n}_l$ , represented by the green arrows in the inset box, should be equal to  $v_{nl}$ . The periodic variations of the local normal direction, therefore, would be manifested by a reversal of the  $v_{nl}$  component along the  $\mathbf{e}_n$  direction ( $v_{nl,n}$ , the black arrows in the inset box) when the local normal direction  $\mathbf{n}_l$  matches  $\mathbf{e}_n$ . These expectations agree with the observations (compare Figures 2f–2h). Moreover, the components of  $\mathbf{n}_l$  and  $\mathbf{v}_{nl}$  along the  $\mathbf{e}_{t2}$  direction show negligible variations around zero in Figures 2f and 2h, which also implies that the surface wave propagation is mostly along the  $\mathbf{e}_{t1}$  axis and thereby justifies our assumption above. A notable exception happens after 02:46:02 UT (the final time interval in Figure 2) when  $n_{l,t2}$  appears to be comparable to  $n_{l,t1}$ , but this may not be real due to the large uncertainty in the  $\mathbf{n}_l$  determination as the three MDD eigenvalues in Figure 2d are comparable during this interval.

One may further estimate the surface wave propagation speed,  $v_s$ , based on the projection relationship discussed above. Since the  $\mathbf{v}_{nl}$  vectors are projections of  $\mathbf{v}_s$  along the local normal directions, the vector-end points of  $\mathbf{v}_{nl}$  (or equivalently, the  $(v_{nl,t1}, v_{nl,t2}, v_{nl,n})$  points in the SAC system) should all be located on a sphere that intersects the origin, of which the diameter is  $v_s$  (see Zhou et al., 2006, Figure 5). A least squares method can thus be used, to fit the vector-end points in Figure 2h toward a sphere in the velocity space. Figure 3b shows a two-dimensional slice of the sphere in the  $v_{nl,n}$ - $v_{nl,t1}$  plane, in which the black dots are the vector-end points and the red arrow represents the best-fit result of the surface wave propagation velocity,  $v_s = [322, -330, 10]$  km/s in SAC. In other words, the ripples propagate predominantly along the  $\mathbf{e}_{t1}$  axis at the speed of  $323 \pm 4$  km/s, which is consistent with our prior assumption. This speed is about 2–2.5 times the downstream Alfvén velocity,  $v_{A,d} = 120 \sim 160$  km/s, which is

also consistent with the expected  $v_s/v_{A,d}$  ratio (between 2 and 4) according to the Cluster measurements of bow-shock surface waves (Moullard et al., 2006).

On the other hand, the spatial profile of the shock along the  $\mathbf{e}_n$  direction can be determined by integrating  $v_{nl,n}$  with time (Johlander et al., 2023). Here, we define  $D = 0$  as the position with maximum  $B_t$  at 02:46:02. Then we integrate  $v_{nl,n}$  to determine the normal distance  $D$  as a function of time, and generate the  $D$ - $B_t$  diagram in Figure 3c. The different colors in the figure correspond to the five intervals separated by the field extrema in Figure 2b. The  $B_t$  profiles within different intervals overlap with one another, and the nearly identical profiles indicate that the observed field oscillations are unlikely caused by the shock reformation, a hypothetical process proposed by Madanian et al. (2021). This conclusion is also consistent with previous simulations (Omidi et al., 2021), in which the surface waves are manifested as low-frequency waves.

We further study the spatial distributions of the high-frequency ( $1 \sim 3$  Hz) whistler waves. This could be done by having a scatter plot between  $B_t$  and the wave power (not shown), which indicates that the region of strong wave activity is largely confined within the  $B_t$  range between 8 and 12 nT. Given the monotonic relationship between  $B_t$  and  $D$  (Figure 3c), the whistler waves appear to be stronger near the foot side (see Figure 2a), which is illustrated in Figure 3a by the concentration of the whistler waves (white curves) within the blue area (where the field strength is only slightly larger than that in the unperturbed solar wind). Along the pink trajectory of the virtual spacecraft, the whistler waves (packets 1 and two in Figure 3a) can be intermittently detected near the  $B_t$  maxima when the spacecraft periodically enters the foot regions from the unperturbed solar wind. This scenario explains the reason why the whistler wave packets appear in the same tone as the surface waves, as shown in Figure 1.

However, this relationship appears to break down at  $\sim 02:45:46$ , after which the whistler wave power peaks around the  $B_t$  minima (see, for example, the vertical solid line in Figure 1) and minimizes near the  $B_t$  maxima (see the vertical dashed lines). The reason lies in the deeper penetration of the spacecraft toward the downstream region. In this case, the spacecraft can no longer access the unperturbed solar wind, but moves back and forth between the ramp (the red area in Figure 3a, with larger  $B_t$  values) and the foot regions. Therefore, the observed correlation between the peak wave power and the  $B_t$  minima is also consistent with the scenario that the whistler wave packets are largely concentrated near the foot region. As time proceeds, the whistler waves gradually disappear since the spacecraft moves across the bow shock to reach the magnetosheath at  $\sim 02:46:10$ .

Interestingly, the ion normal-velocity spectrum in Figure 1e displays a phase-space hole structure at 02:46:05. This signature has been commonly used to identify the shock ripples (Gingell et al., 2017; Johlander et al., 2016, 2018), which enable the spacecraft to travel back-and-forth across the bow shock. In other words, the flanks of the ion phase-space hole (before and after the hole center, with enhanced magnetic field strength) are composed of the heated ions in the downstream region. The center of the ion phase-space hole, on the other hand, is constituted by the coexisting solar wind ions and the reflected population at locations closer to the upstream region.

### 3. Discussion and Summary

In this paper, we report the MMS observations of periodic magnetic field enhancements when the spacecraft penetrate the terrestrial bow shock. As mentioned in the introductory section, such observations are often interpreted as signatures of bow shock reformation under extremely high Mach numbers (Madianian et al., 2020, 2021; Sulaiman et al., 2015). However, similar signatures may also be attributed to the rippled shocks in the presence of surface waves. Therefore, it is important to distinguish between spatial and temporal variations (Gingell et al., 2017; Omidi et al., 2021) with the aid of multi-spacecraft observations. In this event, the periodic variations of the local normal directions, together with the overlapped spatial profiles of the magnetic field, provide solid evidence supporting the interpretation of surface waves rather than shock reformation. Given the tremendous divergence of Mach numbers in the observations of possible shock reformation events (Johlander et al., 2016; Madanian et al., 2021), it is probably worth revisiting those events and distinguishing these two potential processes before a statistical investigation is carried out on the associated parameter regimes (Sulaiman et al., 2015). This will be done in a future study.

We also discuss the relationship among shock surface waves, whistler waves, and reflected ions. In our event, the reflected ions are largely confined near the foot region of the quasi-perpendicular bow shock, which provide the free energy for the excitation of the whistler waves (Lalti et al., 2022). The surface waves, on the other hand, could twist the shock structure to spatially modulate the distributions of the reflected ions, and consequently, the

whistler wave packets. This simple scenario, however, may not be the full story. For example, it has been suggested in Omidi et al. (2021) that the ion reflection could lead to large velocity shears that contribute to the surface wave excitation. The resulting shock ripples, according to Khotyaintsev et al. (2023), could be associated with large-amplitude, normal electric field structures and contribute to the ion reflection process. Moreover, the propagation of the surface waves could modify the magnetic field configuration near the shock front, which in turn could adjust the nonlinear growth of the whistler waves (Omura, 2021).

Interestingly, it has been proposed that whistler waves could play an important role in the formation of new shock fronts at the foot region (Matsukiyo & Scholer, 2006; Scholer et al., 2003), which is made possible by the deceleration and thermalization of the reflected ions as they interact with the whistler waves. Therefore, the interplay between surface waves and whistler waves may even influence the shock reformation process. In fact, the reformation of a rippled, quasi-perpendicular shock has been shown to coexist with the whistler waves in a hybrid simulation (Yuan et al., 2009). For quasi-parallel shocks, the coexistence and interaction between shock reformation and surface waves have also been proposed (Gingell et al., 2017; Hao et al., 2017). In other words, the plasma environments in the adjacency of quasi-perpendicular bow shocks are highly coupled due to coexistence of various plasma waves and multiple particle populations. A more systematic investigation is required to understand the complicated interplay of these plasma components and the associated energy transfer processes.

## Data Availability Statement

All MMS data are available to the public via <https://lasp.colorado.edu/mms/sdc/public/>. The MMS data are processed and analyzed using the IRFU-Matlab package available at <https://github.com/irfu/irfu-matlab>. The MDD and STD analysis results are deposited in Li and Zhou (2024).

## Acknowledgments

We are grateful to the MMS mission and team for the high-resolution measurements of the particles and fields. This work is supported by the National Natural Science Foundation of China Grants 42174184.

## References

- Archer, M., Hartinger, M., Plaschke, F., Southwood, D., & Rastaetter, L. (2021). Magnetopause ripples going against the flow form azimuthally stationary surface waves. *Nature Communications*, 12(1), 5697. <https://doi.org/10.1038/s41467-021-25923-7>
- Archer, M., Hietala, H., Hartinger, M. D., Plaschke, F., & Angelopoulos, V. (2019). Direct observations of a surface eigenmode of the dayside magnetopause. *Nature Communications*, 10(1), 615. <https://doi.org/10.1038/s41467-018-08134-5>
- Caprioli, D., Pop, A.-R., & Spitkovsky, A. (2014). Simulations and theory of ion injection at non-relativistic collisionless shocks. *The Astrophysical Journal Letters*, 798(2), L28. <https://doi.org/10.1088/2041-8205/798/2/L28>
- Dimmock, A. P., Russell, C. T., Sagdeev, R. Z., Krasnoselskikh, V., Walker, S. N., Carr, C., et al. (2019). Direct evidence of nonstationary collisionless shocks in space plasmas. *Science Advances*, 5(2), eaau9926. <https://doi.org/10.1126/sciadv.aau9926>
- Dudok de Wit, T., Krasnosel'skikh, V., Bale, S., Dunlop, M., Lühr, H., Schwartz, S., & Woolliscroft, L. (1995). Determination of dispersion relations in quasi-stationary plasma turbulence using dual satellite data. *Geophysical Research Letters*, 22(19), 2653–2656. <https://doi.org/10.1029/95gl02543>
- Gingell, I., Schwartz, S. J., Burgess, D., Johlander, A., Russell, C. T., Burch, J. L., et al. (2017). MMS observations and hybrid simulations of surface ripples at a marginally quasi-parallel shock. *Journal of Geophysical Research: Space Physics*, 122(11), 11–023. <https://doi.org/10.1002/2017ja024538>
- Hao, Y., Gao, X., Lu, Q., Huang, C., Wang, R., & Wang, S. (2017). Reformation of rippled quasi-parallel shocks: 2-d hybrid simulations. *Journal of Geophysical Research: Space Physics*, 122(6), 6385–6396. <https://doi.org/10.1002/2017JA024234>
- He, F., Guo, R.-L., Dunn, W. R., Yao, Z.-H., Zhang, H.-S., Hao, Y.-X., et al. (2020). Plasmapause surface wave oscillates the magnetosphere and diffuse aurora. *Nature Communications*, 11(1), 1668. <https://doi.org/10.1038/s41467-020-15506-3>
- Johlander, A., Khotyaintsev, Y. V., Dimmock, A. P., Graham, D. B., & Lalti, A. (2023). Electron heating scales in collisionless shocks measured by MMS. *Geophysical Research Letters*, 50(5), e2022GL100400. <https://doi.org/10.1029/2022gl100400>
- Johlander, A., Schwartz, S., Vaivads, A., Khotyaintsev, Y. V., Gingell, I., Peng, I., et al. (2016). Rippled quasiperpendicular shock observed by the magnetospheric multiscale spacecraft. *Physical Review Letters*, 117(16), 165101. <https://doi.org/10.1103/physrevlett.117.165101>
- Johlander, A., Vaivads, A., Khotyaintsev, Y. V., Gingell, I., Schwartz, S. J., Giles, B. L., et al. (2018). Shock ripples observed by the MMS spacecraft: Ion reflection and dispersive properties. *Plasma Physics and Controlled Fusion*, 60(12), 125006. <https://doi.org/10.1088/1361-6587/aae920>
- Kennel, C., Edmiston, J., & Hada, T. (1985). A quarter century of collisionless shock research. *Geophysical Monograph Series*, 34, 1–36. <https://doi.org/10.1029/gm034p0001>
- Khotyaintsev, Y. V., Graham, D. B., & Johlander, A. (2023). Ion reflection by a rippled perpendicular shock. Arxiv Preprints. <https://doi.org/10.48550/arXiv.2312.14736>
- Krasnoselskikh, V., Lembège, B., Savoini, P., & Lobzin, V. (2002). Nonstationarity of strong collisionless quasiperpendicular shocks: Theory and full particle numerical simulations. *Physics of Plasmas*, 9(4), 1192–1209. <https://doi.org/10.1063/1.1457465>
- Lalti, A., Khotyaintsev, Y. V., Graham, D. B., Vaivads, A., Steinvall, K., & Russell, C. T. (2022). Whistler waves in the foot of quasi-perpendicular supercritical shocks. *Journal of Geophysical Research: Space Physics*, 127(5), e2021JA029969. <https://doi.org/10.1029/2021ja029969>
- Li, J.-H., & Zhou, X.-Z. (2024). Data for "Bow shock ripples and their modulation of whistler wave packets: MMS observations. [dataset]. Zenodo. <https://doi.org/10.5281/zenodo.1337745>
- Li, J.-H., Zhou, X.-Z., Liu, Z.-Y., Wang, S., Artemyev, A. V., Omura, Y., et al. (2024). Identification of coupled Landau and anomalous resonances in space plasmas. *Physical Review Letters*, 133(3), 035201. <https://doi.org/10.1103/PhysRevLett.133.035201>

- Li, J.-H., Zhou, X.-Z., Liu, Z.-Y., Wang, S., Omura, Y., Li, L., et al. (2024). Direct observations of cross-scale energy transfer in space plasmas. Arxiv Preprints. <https://doi.org/10.48550/arXiv.2406.05744>
- Lowe, R., & Burgess, D. (2003). The properties and causes of rippling in quasi-perpendicular collisionless shock fronts. *Annales Geophysicae*, 21(3), 671–679. <https://doi.org/10.5194/angeo-21-671-2003>
- Madanian, H., Desai, M., Schwartz, S., Wilson, L., Fuselier, S., Burch, J., et al. (2021). The dynamics of a high mach number quasi-perpendicular shock: MMS observations. *The Astrophysical Journal*, 908(1), 40. <https://doi.org/10.3847/1538-4357/abc88>
- Madanian, H., Schwartz, S. J., Halekas, J. S., & Wilson, L. B. (2020). Nonstationary quasiperpendicular shock and ion reflection at mars. *Geophysical Research Letters*, 47(11), e2020GL088309. <https://doi.org/10.1029/2020GL088309>
- Malkov, M., Diamond, P., & Sagdeev, R. (2011). Mechanism for spectral break in cosmic ray proton spectrum of supernova remnant w44. *Nature Communications*, 2(1), 194. <https://doi.org/10.1038/ncomms1195>
- Matsukiyo, S., & Scholer, M. (2006). On reformation of quasi-perpendicular collisionless shocks. *Advances in Space Research*, 38(1), 57–63. <https://doi.org/10.1016/j.asr.2004.08.012>
- Morse, D., Destler, W., & Auer, P. (1972). Nonstationary behavior of collisionless shocks. *Physical Review Letters*, 28(1), 13–16. <https://doi.org/10.1103/physrevlett.28.13>
- Moullard, O., Burgess, D., Horbury, T., & Lucek, E. (2006). Ripples observed on the surface of the earth's quasi-perpendicular bow shock. *Journal of Geophysical Research*, 111(A9). <https://doi.org/10.1029/2005ja011590>
- Omidi, N., Desai, M., Russell, C., & Howes, G. (2021). High mach number quasi-perpendicular shocks: Spatial versus temporal structure. *Journal of Geophysical Research: Space Physics*, 126(9), e2021JA029287. <https://doi.org/10.1029/2021ja029287>
- Omura, Y. (2021). Nonlinear wave growth theory of whistler-mode chorus and hiss emissions in the magnetosphere. *Earth Planets and Space*, 73, 1–28. <https://doi.org/10.1186/s40623-021-01380-w>
- Pitňa, A., Šafránková, J., Němeček, Z., Ďurovcová, T., & Kis, A. (2021). Turbulence upstream and downstream of interplanetary shocks. *Frontiers in Physics*, 8, 626768. <https://doi.org/10.3389/fphy.2020.626768>
- Pollock, C., Moore, T., Jacques, A., Burch, J., Gliese, U., Saito, Y., et al. (2016). Fast plasma investigation for magnetospheric multiscale. *Space Science Reviews*, 199, 331–406.
- Russell, C., Anderson, B., Baumjohann, W., Bromund, K., Dearborn, D., Fischer, D., et al. (2016). Others (2016). The magnetospheric multiscale magnetometers. *Space Science Reviews*, 199(1–4), 189–256. <https://doi.org/10.1007/s11214-014-0057-3>
- Scholer, M., Shinohara, I., & Matsukiyo, S. (2003). Quasi-perpendicular shocks: Length scale of the cross-shock potential, shock reformation, and implication for shock surfing. *Journal of Geophysical Research*, 108(A1), SSH-4. <https://doi.org/10.1029/2002ja009515>
- Schwartz, S. J. (1998). Shock and discontinuity normals, mach numbers, and related parameters. *ISSI Scientific Reports Series*, 1, 249–270.
- Scudder, J., Mangeney, A., Lacombe, C., Harvey, C., Aggson, T., Anderson, R., et al. (1986). The resolved layer of a collisionless, high  $\beta_{\text{beta}}$ , supercritical, quasi-perpendicular shock wave: 1. Rankine-hugoniot geometry, currents, and stationarity. *Journal of Geophysical Research*, 91(A10), 11019–11052. <https://doi.org/10.1029/ja091ia10p11019>
- Shi, Q., Shen, C., Dunlop, M., Pu, Z., Zong, Q.-G., Liu, Z., et al. (2006). Motion of observed structures calculated from multi-point magnetic field measurements: Application to cluster. *Geophysical Research Letters*, 33(8). <https://doi.org/10.1029/2005gl025073>
- Shi, Q., Shen, C., Pu, Z., Dunlop, M., Zong, Q.-G., Zhang, H., et al. (2005). Dimensional analysis of observed structures using multipoint magnetic field measurements: Application to cluster. *Geophysical Research Letters*, 32(12). <https://doi.org/10.1029/2005gl022454>
- Sulaiman, A., Masters, A., Dougherty, M., Burgess, D., Fujimoto, M., & Hospodarsky, G. (2015). Quasiperpendicular high mach number shocks. *Physical Review Letters*, 115(12), 125001. <https://doi.org/10.1103/physrevlett.115.125001>
- Torbert, R., Russell, C., Magnes, W., Ergun, R., Lindqvist, P.-A., LeContel, O., et al. (2016). The fields instrument suite on MMS: Scientific objectives, measurements, and data products. *Space Science Reviews*, 199(1–4), 105–135. <https://doi.org/10.1007/s11214-014-0109-8>
- Umeda, T., Yamao, M., & Yamazaki, R. (2009). Electron acceleration at a low mach number perpendicular collisionless shock. *The Astrophysical Journal*, 695(1), 574–579. <https://doi.org/10.1088/0004-637x/695/1/574>
- Wang, S., Chen, L.-J., Bessho, N., Hesse, M., Giles, B. L., & Moore, T. E. (2019). Ion behaviors in the reconnection diffusion region of a corrugated magnetotail current sheet. *Geophysical Research Letters*, 46(10), 5014–5020. <https://doi.org/10.1029/2019gl082226>
- Wang, S., Li, J.-H., Li, L., Zhou, X.-Z., Omura, Y., Zhao, J., et al. (2024). A statistical examination of ion dynamics at 1-hz whistler waves in Earth's foreshock. *Journal of Geophysical Research: Space Physics*, 129, e2024JA032960. <https://doi.org/10.1029/2024JA032960>
- Wilson, L. B. (2016). Low frequency waves at and upstream of collisionless shocks. *Low-frequency waves in space plasmas*, 269–291. <https://doi.org/10.1002/9781119055006.ch16>
- Wilson, L. B., Sibeck, D. G., Breneman, A. W., Contel, O. L., Cully, C., Turner, D. L., et al. (2014a). Quantified energy dissipation rates in the terrestrial bow shock: 1. Analysis techniques and methodology. *Journal of Geophysical Research: Space Physics*, 119(8), 6455–6474. <https://doi.org/10.1002/2014ja019929>
- Wilson, L. B., Sibeck, D. G., Breneman, A. W., Contel, O. L., Cully, C., Turner, D. L., et al. (2014b). Quantified energy dissipation rates in the terrestrial bow shock: 2. Waves and dissipation. *Journal of Geophysical Research: Space Physics*, 119(8), 6475–6495. <https://doi.org/10.1002/2014ja019930>
- Winske, D., & Quest, K. (1988). Magnetic field and density fluctuations at perpendicular supercritical collisionless shocks. *Journal of Geophysical Research*, 93(A9), 9681–9693. <https://doi.org/10.1029/ja093ia09p09681>
- Yuan, X., Cairns, I. H., Trichtchenko, L., Rankin, R., & Danksin, D. W. (2009). Confirmation of quasi-perpendicular shock reformation in two-dimensional hybrid simulations. *Geophysical Research Letters*, 36(5). <https://doi.org/10.1029/2008GL036675>
- Zhou, X.-Z., Zong, Q., Pu, Z., Fritz, T., Dunlop, M., Shi, Q., et al. (2006). Multiple triangulation analysis: Another approach to determine the orientation of magnetic flux ropes. *Annals of Geophysics*, 24(6), 1759–1765. <https://doi.org/10.5194/angeo-24-1759-2006>